Chemical Science

ROYAL SOCIETY OF CHEMISTRY

EDGE ARTICLE

View Article Online
View Journal

Cite this: DOI: 10.1039/d6sc00466k

All publication charges for this article have been paid for by the Royal Society of Chemistry

Point-to-volume engineering enables enhanced birefringence and a wide bandgap in hybrid halide ultraviolet nonlinear optical crystals

Jiajing Wu,*[a] Ruo-Nan Li,[a] Wen-Dong Yao,[a] Yi-Fan Fu[ab] and Sheng-Ping Guo *[ab]

Ultraviolet nonlinear optical (UV NLO) crystals are important for advanced photonics, yet their development is hindered by the inherent trade-off among strong SHG response, a wide bandgap and large birefringence. Herein, guided by systematic theoretical screening, the "two-in-one" flexible π-conjugated $(C_4H_{13}N_5)^{2+}$ (**MF**) group was identified as a prospective functional building unit (FBU) owing to its superior polarizability anisotropy and hyperpolarizability. Its initial combination with Cl^- yielded $C_4H_{13}N_5Cl_2$ (**MFC**), which exhibits a wide band gap (4.64 eV) and a high SHG response (2.8 × KH_2PO_4 (KDP)), yet a small birefringence of 0.02@546 nm. To address this limitation, we implemented a point-to-volume substitution strategy, replacing the discrete Cl^- anions in **MFC** with distorted $[ZnCl_4]^{2-}$ tetrahedra, yielding a novel zero-dimensional (0D) organic–inorganic hybrid halide $(C_4H_{13}N_5)ZnCl_4$ (**MFZC**). This structural evolution simultaneously enhances most of the key optical properties: bandgap widening to 4.72 eV, birefringence enhancement to 0.09 at 546 nm, and retention of a strong SHG response of 2.2 × KDP. Theoretical and structural analyses indicate that the improved properties originate from the synergistic alignment of organic **MF** cations and inorganic $[ZnCl_4]^{2-}$ tetrahedral FBUs. This work provides an effective strategy for engineering hybrid halide materials with concurrently optimized linear and nonlinear optical properties.

Received 16th January 2026
Accepted 15th April 2026

DOI: 10.1039/d6sc00466k

rsc.li/chemical-science

Introduction

Nonlinear optical (NLO) crystals are indispensable for frequency conversion in solid-state lasers,[1,2] enabling the generation of coherent light and extending the operational wavelength into the short-wavelength ultraviolet (UV) region.[3–5] Their functionality is critical for key applications including precision micromachining, modern medical treatment, and information storage.[6–9] However, high-performance commercial UV NLO materials are rather scarce, with representative ones including β-BaB_2O_4 (β-BBO),[10] LiB_3O_5 (LBO),[11] and $KBe_2BO_3F_2$ (KBBF).[12] Excellent UV NLO materials must achieve an effective balance among large second-harmonic generation (SHG) effects, a wide bandgap and appropriate birefringence.[13–15] These properties, however, are mutually constrained, making their concurrent optimization within a single crystal a persistent challenge. To achieve balance, researchers are paying increasing attention to the rational structure design of such materials.[16]

The rational design of structural motifs and the deliberate choice of their assembly modes serve as the key background for optimizing NLO properties. Inorganic π-conjugated groups, such as $(BO_3)^{3-}$,[17] $(NO_3)^-$,[18] and $(B_3O_6)^{3-}$,[19] serve as superior UV NLO-active building units and exhibit strong polarizability anisotropy (δ) and large hyperpolarizability tensor ($\beta_{|max|}$). These features have enabled the development of notable NLO crystals, including KBBF,[12] $RE(OH)_2NO_3$ (RE = La, Y, Gd),[20] and $Ba_2Mg(B_3O_6)_2$ (BMBO).[21] However, the growth of inorganic NLO crystals is typically associated with high costs, substantial energy consumption, and prolonged processing times.[22] Studies have shown that organic π-conjugated groups, such as $(C_3N_3S_3H_x)^{x-3}$ (x = 0–3),[23–26] $[C(NH_2)_3]^+$ (Gua^+),[2,27] ($DAMS^+$),[28] *etc.*, outperform their structurally similar inorganic counterparts in both second-order polarizability and optical anisotropy.[16] For example, the large delocalized π-electron systems of $Cd(SCN)_2(C_4H_6N_2)_2$ (10 × KDP, E_g = 4.74 eV),[29] $ZnBr(C_6H_{3.5}FNO_2)_2$ (1.7 × KDP, E_g = 4.2 eV),[30] $(C_5H_6N_2O_2)ZnCl_2$ (3.5 × KDP, E_g = 5.19 eV),[31] and $[C(NH_2)_3]_3PO_4\cdot 2H_2O$ (1.5 × KDP, E_g = 4.2 eV)[2] can effectively balance the critical performance metrics indispensable for short-wave UV NLO crystals.

The coupling of functional groups (*e.g.*, dimeric $[B_2O_5]^{4-}$ and $[P_2O_7]^{4-}$) is recognized as an effective strategy for enhancing SHG efficiency.[32] However, achieving precise and controllable coupling in inorganic systems remains synthetically challenging,[33] whereas such coupling can be more readily and predictably realized in organic frameworks.[34] Inspired by reported examples such as $M_4Mg_4(P_2O_7)_3$ (M = K, Rb),[33] NH $[C(NH_2)_2]_2(NO_3)_2$,[16] $\{N[C(NH_2)_2]_2\}_2CO_3$,[16] and $[C_2N_4H_7O]$

[a]School of Chemistry and Materials, Yangzhou University, Yangzhou, Jiangsu 225002, P. R. China. E-mail: spguo@yzu.edu.cn; jiajingw@yzu.edu.cn

[b]School of Materials and Energy, Yunnan University, Kunming 650500, P. R. China

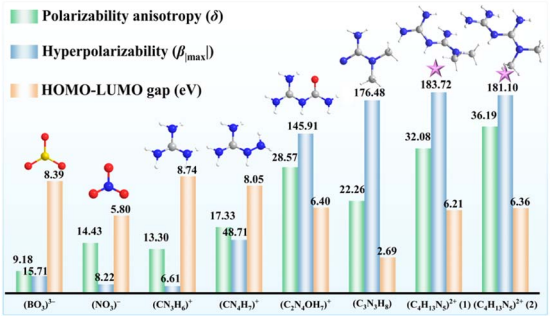

Fig. 1 Calculated gaps between the highest occupied molecular orbital (HOMO) and the lowest unoccupied molecular orbital (LUMO), polarizability anisotropy (δ), and the maximum absolute value of hyperpolarizability ($\beta_{|max|}$) of typical functional groups.

$[NH_2SO_3]$,[32] we have identified a flexible "two-in-one" organic group, metformin ($[C_4H_{13}N_5]^{2+}$, abbreviated **MF**), which is formed by combining planar $[C(NH_2)_3]^+$ and $[C(NH_2)_3(CH_3)_2]$ through a shared nitrogen atom. Theoretical calculations reveal that the π-conjugated **MF** cation exhibits favorable δ values and a large $\beta_{|max|}$, exceeding those of well-known building units such as $[BO_3]^{3-}$,[17] $(NO_3)^-$,[18] $(C_2N_4OH_7)^+$,[32] *etc.* (Fig. 1). These results demonstrate that the **MF** moiety represents a highly promising functional building block for the design of nonlinear optical crystals.

Based on the anionic group theory,[35] the rational introduction of halide anions or their assembled metal-halide polyhedral units serves as a key molecular design strategy for developing high-performance NLO crystals. Halide anions (Cl^-, Br^-, and I^-), with their high electronegativity and strong polarizability, can effectively widen the optical bandgap and enhance the macroscopic polarization of the crystal lattice, such as Mg_2PO_4Cl[36] and $Ba_3P_3O_{10}Cl$.[37] When coordinated with metal cations with stereochemically active lone pairs (Pb^{2+}, Sb^{3+}, and Te^{4+}) or d^{10} electron configurations (Cd^{2+} and Zn^{2+}), they form structurally distorted metal-halogen polyhedra, which not only break the structural symmetry but also provide a large microscopic second-order susceptibility. Examples include (L-ipp)(L-pro)PbI_3,[38] $(C_5H_6N_2O_2)ZnBr_2$,[31] and [DASH]Cd_2Cl_6.[28]

Guided by this strategy, we have successfully synthesized $C_4H_{13}N_5Cl_2$ (**MFC**) through the rational integration of the distinctive merits of organic cations $(C_4H_{13}N_5)^{2+}$ (1) (Fig. 1). Although **MFC** was initially reported in 2023,[39] its optical properties have not yet been systematically investigated. Meanwhile, by employing a novel point-to-volume substitution strategy—replacing the discrete Cl^- ions in **MFC** with $[ZnCl_4]^{2-}$ tetrahedral units—we have obtained a new UV NLO crystal $(C_4H_{13}N_5)ZnCl_4$ (**MFZC**). Both **MFC** and **MFZC** exhibit wide bandgaps (>4.6 eV) and strong SHG responses (>2 × KDP). Notably, the birefringence value of **MFZC** exhibits a 4.5 times enhancement relative to that of **MFC** because **MFZC** features a significantly higher degree of structural ordering compared with **MFC**. Here, we present a systematic investigation into the synthesis, crystal structures, optical properties, theoretical calculations, and structure-property relationships of **MFC** and **MFZC**.

Results and discussion

The colorless and transparent crystals of **MFC** (rod-shaped) and **MFZC** (block-shaped) were obtained *via* slow solvent evaporation at room temperature (Fig. 2a). Their crystal structures were confirmed by single-crystal X-ray diffraction (SCXRD) analysis, and detailed crystallographic data are summarized in Tables S1–S5 (SI). Both **MFC** and **MFZC** crystallize in the monoclinic polar noncentrosymmetric (NCS) space group $P2_1$ (No. 4) and feature zero-dimensional (0D) structures (Fig. 2c and d). The phase purities of **MFC** and **MFZC** were confirmed by powder X-ray diffraction (PXRD) analysis (Fig. S1).

For **MFC**, its asymmetric unit contains one protonated **MF** cation and two free Cl^- anions (Fig. S2). The **MF** unit exhibits a "two-in-one" flexible configuration, comprising planar $[CN_3H_5]$ and $[C_3N_3H_8]$ groups (Fig. 2b). The dihedral angle between them, denoted as α, is 63.01° in **MFC**. As shown in Fig. S3, the organic **MF** molecules and Cl^- anions are interconnected *via* hydrogen bonds in the *ab*-plane, forming a *pseudo*-2D structure. The layers stack along the *c*-axis, resulting in a *pseudo*-3D network framework. Along the *c*-axis, the organic molecules **MF** exhibit an alternating -ABAB- arrangement. The dihedral angles between adjacent organic cations in layer A and layer B were determined to be $\beta_1 = 80.48°$ (between two $[CN_3H_5]$ planes) and $\beta_2 = 77.76°$ (between two $[C_3N_3H_8]$ planes), respectively, with an interlayer distance of 7.50 Å (Fig. 2f). Within layer A or layer B, adjacent organic cations aligned along the *b*-axis exhibit a dihedral angle of 0° and an interatomic spacing of 5.79 Å (Fig. 2f). The organic **MF** cation is tilted relative to the (001) crystal plane with a dihedral angle (γ) of 86.37° (Fig. S7a). To further evaluate the interplay of molecular interactions in the structure of **MFC**, we employed Hirshfeld surface (HS) analysis and mapped d_{norm}, which are presented in Fig. 2e. The red areas on the Hirshfeld surface correspond to significant H···Cl contacts (Fig. 2e). The percentage contribution of H···Cl interaction is 45.6% for **MFC** (Fig. 2e and S6a).

In contrast to **MFC**, the Cl^- anions in **MFZC** are not free ions but coordinate to Zn atoms, forming tetrahedral $[ZnCl_4]^{2-}$ units. The asymmetric unit of **MFZC** consists of one such $[ZnCl_4]^{2-}$ tetrahedron and one protonated **MF** cation (Fig. S4). The dihedral angle (α) within the **MF** unit decreases from 63.01° to 53.15°. **MFZC** also adopts a *pseudo*-layered structure parallel to the *ab* plane, wherein the $(C_4H_{13}N_5)^{2+}$ cations and $[ZnCl_4]^{2-}$ anions are interconnected by [N–H···Cl] and [C–H···Cl] hydrogen bonds, with the H···Cl distances ranging from 2.47 to 2.79 Å (Fig. S5 and Table S5). These *pseudo*-layers stack along the *c* direction to form the entire 3D network of **MFZC** (Fig. S5). Similar to **MFC**, the organic moieties **MF** in **MFZC** adopt an alternating "ABAB" arrangement along the *c*-axis, with an interlayer distance of 7.91 Å (Fig. 2g). Notably, within the organic **MF** cations in **MFZC**, the $[C_3N_3H_8]$ adopts a *zig-zag* arrangement with $\beta_2 = 76.17°$, whereas $[CN_3H_5]$ groups exhibit $\beta_1 = 15.12°$ and an interatomic spacing of 6.92 Å. The H···Cl ratio of these hydrogen bonds is higher in **MFZC** than in **MFC** (Fig. 2e and h). These enhanced hydrogen-bonding interactions

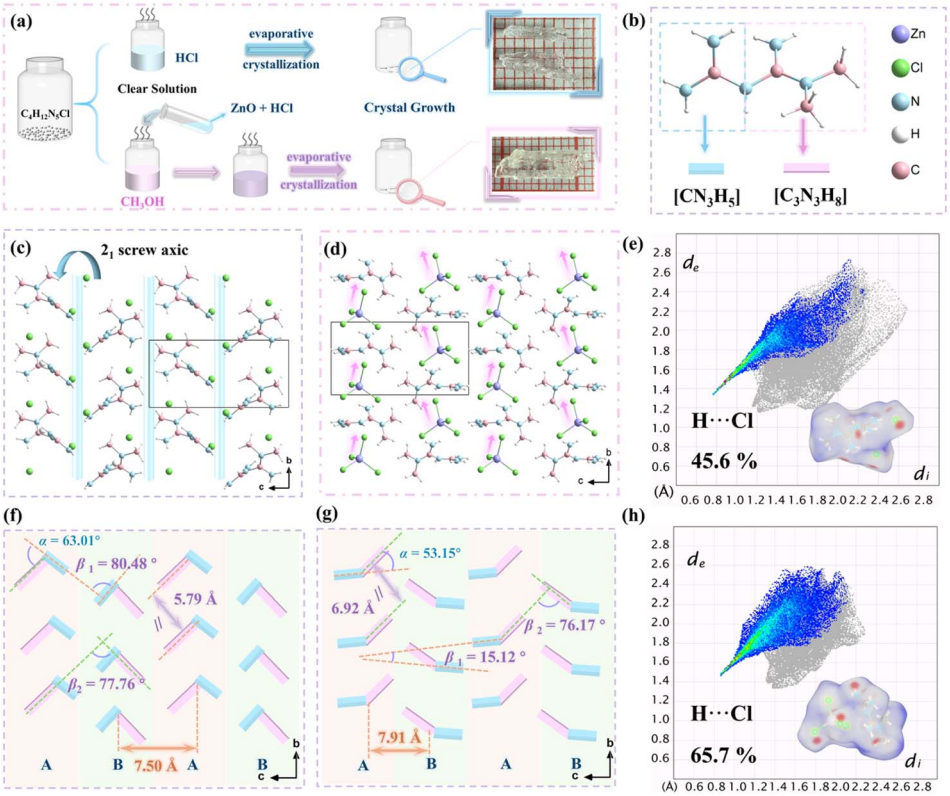

Fig. 2 (a) The synthesis of **MFC** and **MFZC**. (b) Functional motifs in **MF**. The crystal structures of (c) **MFC** and (d) **MFZC**. Hirshfeld surfaces for (e) **MFC** and (h) **MFZC**. Modular description of functional motifs for (f) **MFC** and (g) **MFZC**.

impose strong structural constraints on the cationic framework, effectively restricting the relative orientation between adjacent organic planes and reducing the dihedral angles. This ordered alignment significantly enhances the overall birefringence of **MFZC** (Fig. 2g). Additionally, the **MF** cations are oriented off the (001) crystal plane with a dihedral angle of $\gamma_2 = 80.28°$ for **MFZC**, which is smaller than that of **MFC** ($\gamma_1 = 86.37°$) (Fig. S7b). This structural feature further enhances the optical anisotropy of **MFZC**. The red regions in the 2D fingerprint plots of hydrogen bonds correspond to H···Cl contacts, accounting for 65.7% of the total interaction. This proportion, which is greater than **MFC** (45.6%), underscores the critical role of hydrogen bonds in stabilizing the structure framework (Fig. 2h and S6b).

The UV-vis-NIR diffuse reflectance spectra demonstrate that the UV cutoff edge of **MFC** is located at 250 nm, while **MFZC** shows a blue-shifted edge at approximately 240 nm (Fig. 3a and b). The corresponding optical bandgap values were determined to be 4.64 eV for **MFC** and 4.72 eV for **MFZC**, consistent with the colorless and transparent appearance of the crystals (Fig. 2a). Notably, the bandgap of **MFZC** surpasses that of previously reported hybrid Zn-based halide NLO crystals including (4-AMP) $ZnX_4 \cdot H_2O$ (X = Cl, Br),[5] (3-AMP)$ZnBr_4$,[40] $(C_4H_{11}N_2)ZnI_3$ [41] and $(C_6H_5N_2)_2ZnCl_4$.[42] The NCS structures of **MFC** and **MFZC** motivated the evaluation of their SHG responses at 1064 nm using the Kurtz–Perry method,[43] with commercially available KDP serving as the reference. As shown in Fig. 3d and e, **MFC** and **MFZC** exhibit strong SHG responses, reaching 2.8 × and 2.2 × KDP, respectively. Furthermore, as the particle size increases, their SHG intensities increase significantly, indicating that they both exhibit phase-matching behaviors. Notably, **MFC** demonstrates more outstanding SHG properties than the majority of metal-free materials, such as $C_5H_6N_3O_2I$,[44] $C(NH_2)_3(I_3O_8)(HI_3O_8)(H_2I_2O_6)(HIO_3)_4 \cdot 3H_2O$[45] and $[C_5H_6O_2N_3]_2[IO_3]_2$.[46] In addition, **MFZC** demonstrates better SHG performance than most similar organic–inorganic zinc-based hybrid materials, like $(C_{14}H_{14}N_2)ZnCl_4$,[47] $(C_6H_{16}N_2)_3Zn_3Br_{12} \cdot 2H_2O$,[48] $(C_4H_{11}N_2)ZnCl_3$ [41] and $(C_{13}N_3H_{14})_2ZnBr_4$ [49] (Fig. 3g and Table S6). The wide bandgaps and strong SHG responses of **MFC** and **MFZC** make them promising UV NLO crystals.

To clarify the structure-property relationships of **MFC** and **MFZC**, the hyperpolarizability of organic moieties and density functional theory (DFT) calculations were conducted. The organic moieties in **MFC** and **MFZC** exhibit the anticipated anisotropy in polarizability, and their hyperpolarizabilities follow the descending order of $\beta_x > \beta_y > \beta_z$ (Fig. 4a and c). As **MFC** and **MFZC** are polar crystals, their polar axes are aligned parallel to the crystallographic *b*-axis along the 2_1 screw axis, a feature dictated by the symmetry of their crystal structures. Consequently, the combined polarizability components along the 2_1 screw axis contribute to the second-order nonlinear optical response.[50] As illustrated in Fig. 4b and d, the hyperpolarizability components of **MFC** and **MFZC** along the 2_1 screw

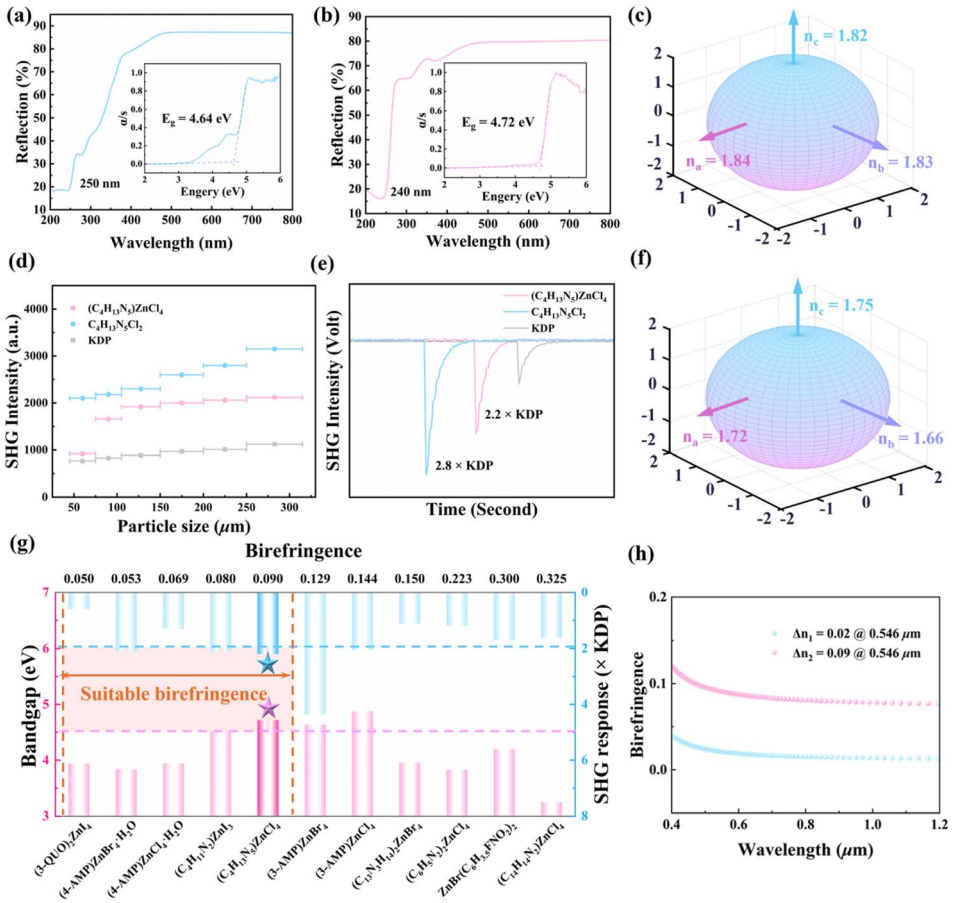

Fig. 3 (a and b) UV-vis spectra of **MFC** (a) and **MFZC** (b). (c and f) Triaxial ellipsoid of three principal refractive indices at 546 nm for (c) **MFC** and (f) **MFZC**. (d) Size-dependent SHG responses of **MFC**, **MFZC** and KDP under 1064 nm laser radiation. (e) SHG intensities of **MFC**, **MFZC** and KDP at 1064 nm. (g) Comparison of bandgaps, SHG efficiency and birefringence in organic–inorganic hybrid zinc-based materials. (h) The calculated birefringence values of **MFC** and **MFZC**.

axis yield values of $\theta_1 = 37.56$ and $\theta_2 = 38.38$, respectively. Furthermore, compared with **MFZC**, **MFC** exhibits a larger hyperpolarizability of the organic $(C_4H_{13}N_5)^{2+}$ molecules (Fig. 1), together with larger dihedral angles β_1 and β_2 between adjacent layers ($\beta_1 = 80.48°$ and $\beta_2 = 77.76°$ for **MFC** and $\beta_1 = 15.12°$ and $\beta_2 = 76.17°$ for **MFZC**) (Fig. 2). These factors collectively contribute to the slightly higher SHG intensity of **MFC** relative to **MFZC**. Meanwhile, the electronic structure analysis indicates that both **MFC** and **MFZC** exhibit indirect bandgaps, with calculated values of 3.62 eV for **MFC** and 3.77 eV for **MFZC** (Fig. 4e and h), where the little underestimation relative to experimental values is attributed to the well-known limitation of the generalized gradient approximation (GGA) in treating exchange-correlation energy discontinuities.[51,52] Since the optical properties of crystalline materials are predominantly determined by electronic transitions near the band edges, we analyzed their total (TDOS) and partial density of states (PDOS) near the Fermi level ($E_f = 0$ eV). The results show that the valence band maximum (VBM) of **MFC** is dominated by Cl 3p states, while that of **MFZC** receives an additional contribution from Zn 3d orbitals. In contrast, the conduction band minimum (CBM) of both compounds is primarily composed of C 2p and N 2p states from the organic **MF** cation. Therefore, the linear and nonlinear optical properties of **MFC** and **MFZC** arise from the synergistic interplay between their organic and inorganic components. Frontier molecular orbital analysis further supports this finding (Fig. 4f and i): the highest occupied molecular orbital (HOMO) is localized on Cl atoms in **MFC** and extends on both Zn 3d and Cl 3p in **MFZC**, whereas the lowest unoccupied molecular orbital (LUMO) in both compounds is dominated by the C 2p and N 2p orbitals of the organic **MF** cation. To gain an in-depth understanding of the microscopic mechanism underlying the NLO properties, the maps of electron localization function (ELF) were studied (Fig. 4g and j). Notably, the electron cloud density around **MF** in **MFC** and **MFZC** exhibits obvious π-conjugated structural features. In addition, there is a significant electron cloud distribution around the Cl^- ions in **MFC** and **MFZC**. Consequently, the **MF** cations and $Cl^-/[ZnCl_4]^{2-}$ anions significantly contribute to their linear and nonlinear optical properties.

The birefringence values of **MFC** and **MFZC** were further evaluated through the first-principles theoretical calculations (Fig. S8 and S9). At 546 nm, the three principal refractive indices of **MFC** and **MFZC** are illustrated in Fig. 3c and f. Specifically, the

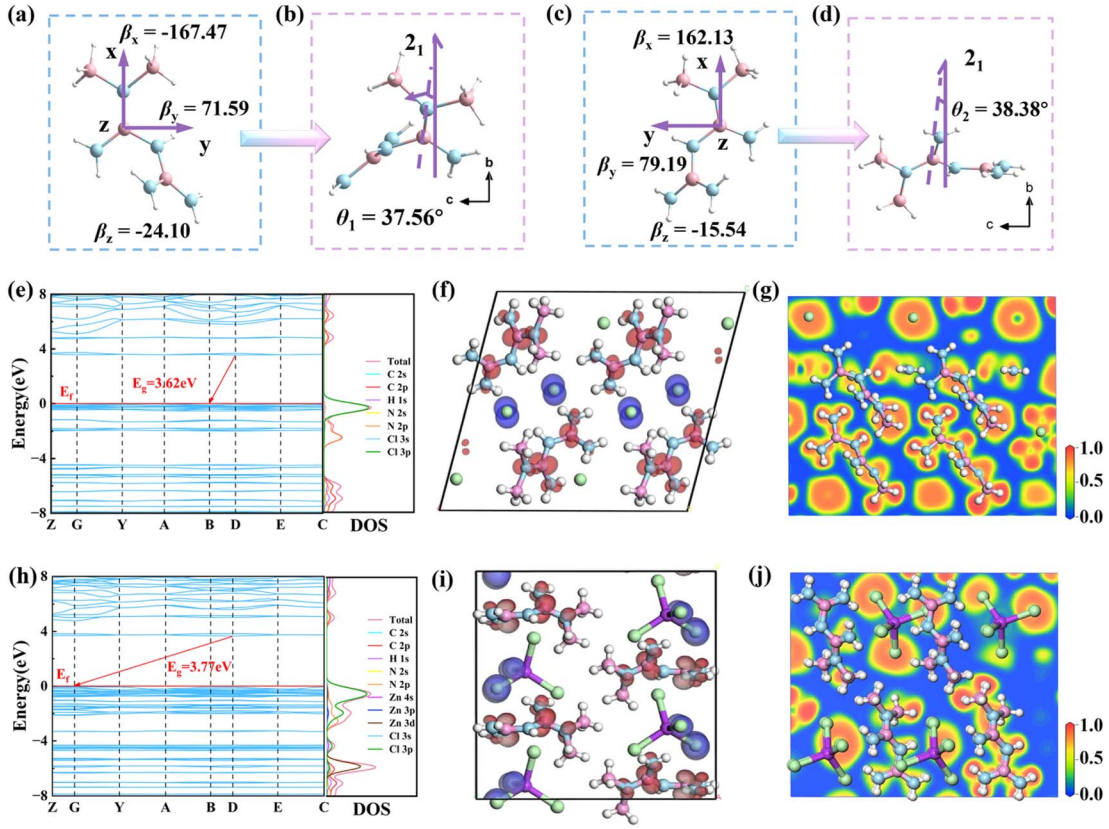

Fig. 4 (a and c) Distribution of the first hyperpolarizability values of organic cations **MFC** and **MFZC**, respectively. Angle (θ) between the β_{max} vector and the crystal polar 2_1 axis in **MFC** (b) and **MFZC** (d). Calculation results: (e and h) calculated band structure and DOS diagrams of (e) **MFC** and (h) **MFZC**. (f and i) The HOMO (blue sector) and LUMO (red sector) maps of (f) **MFC** and (i) **MFZC**. (g and j) The ELF diagrams of (g) **MFC** and (j) **MFZC**.

refractive indices of **MFC** follow the order of $n_a > n_b > n_c$, whereas those of **MFZC** exhibit the sequence $n_c > n_a > n_b$. Their birefringence values are calculated to be 0.02 and 0.09 at 546 nm, respectively (Fig. 3h). It is worth noting that the birefringence of **MFZC** is 4.5 times higher than that of **MFC**, because (i) the organic $(C_4H_{13}N_5)^{2+}$ cations of **MFZC** possess a larger polarizability anisotropy than those of **MFC** (Fig. 1). (ii) The dihedral angle (α) within the **MF** moiety decreases from 63.01° in **MFC** to 53.15° in **MFZC**. (iii) The dihedral angles between adjacent organic cations in the A and B layers of **MFC** are determined to be $\beta_1 = 80.48°$ and $\beta_2 = 77.76°$, respectively. In contrast, for the organic **MF** cations in **MFZC**, the corresponding dihedral angles are $\beta_1 = 15.12°$ and $\beta_2 = 76.17°$ (Fig. 2). (iv) The **MF** cation exhibits an orientation deviation from the (001) plane, with the dihedral angle $\gamma_2 = 80.28°$ for **MFZC** being lower than $\gamma_1 = 86.37°$ for **MFC** (Fig. S7). Furthermore, the birefringence of **MFZC** is larger than those of some commercial crystals and zinc-based hybrid halide crystals, such as MgF_2 (0.012@532 nm),[53] $LiNbO_3$ (0.089@546 nm),[54] and (4-AMP)$ZnX_4 \cdot H_2O$ (X = Cl, Br) (0.069@546 nm and 0.053@546 nm, respectively).[5] Therefore, these data demonstrate that the birefringence values of **MFC** and **MFZC** are predominantly governed by **MF** moieties, highlighting that the coupling of π-conjugated groups represents a meaningful strategy for manipulating the macroscopic optical anisotropy of materials.

Conclusions

In conclusion, this work demonstrates that the metformin cation **MF** is a promising NLO-active functional motif and reports the synthesis of new **MFZC** *via* a point-to-volume substitution strategy from **MFC**. **MFZC** exhibits strong SHG response and a wide optical bandgap. Moreover, the successful introduction of $[ZnCl_4]^{2-}$ tetrahedral units and the favorable arrangement of organic cations collectively enhance the optical anisotropy of **MFZC**, much higher than that of **MFC**. Theoretical calculation and structural analysis demonstrate that the optical properties of **MFC** and **MFZC** are synergistically affected by both organic **MF** cations and inorganic halogen ions/metal-halide anions. This work offers not only a promising UV NLO material, but also an effective strategy for the rational design of novel SHG materials.

Author contributions

This work was conceptualized by Jiajing Wu. Experimentation was performed by Ruo-Nan Li. Software analysis was performed by Wen-Dong Yao. Besides, Jiajing Wu and Sheng-Ping Guo contributed to funding acquisition and supervision. The first draft of the manuscript was prepared by Jiajing Wu and Ruo-Nan Li, and the final draft was edited by all the authors.

Conflicts of interest

The authors declare that they have no conflict of interest.

Data availability

The data supporting this article have been included as part of the supplementary information (SI). Supplementary information: additional tables and pictures. See DOI: https://doi.org/10.1039/d6sc00466k.

CCDC 2521794 $C_4H_{13}N_5Cl_2$ and 2522224 $(C_4H_{13}N_5)ZnCl_4$ contain the supplementary crystallographic data for this paper.[55a,b]

Acknowledgements

This work was supported by the National Natural Science Foundation of China (22505217 and 22371246), the Natural Science Foundation of Jiangsu Province (Grant No. BK20220558), the Yangzhou University Science and Technology Innovation Fund (2022CXJ029), the start-up fund of Yangzhou University (Grant No. 137012279) and the Lvyangjinfeng Talent Program of Yangzhou (YZLYJFJH2021YXBS085).

Notes and references

1 S. Zhao, P. Gong, L. Bai, X. Xu, S. Zhang, Z. Sun, Z. Lin, M. Hong, C. Chen and J. Luo, *Nat. Commun.*, 2014, **5**, 4019.
2 X. Wen, C. Lin, M. Luo, H. Fan, K. Chen and N. Ye, *Sci. China Mater.*, 2021, **64**, 2008–2016.
3 D. F. Eaton, *Science*, 1991, **253**, 281–287.
4 N. Savage, *Ultraviolet Lasers, Nat. Photonics.*, 2007, **1**, 83–85.
5 C. Shen, C. Zhang, Q. Xing, D. Sun, K. Wu, B. Zhang, J. Wang and D. Wang, *Chem. Eng. J.*, 2025, **509**, 161389.
6 H. Fan, N. Ye and M. Luo, *Acc. Chem. Res.*, 2023, **56**, 3099–3109.
7 S. Choi, Y. Li, Y. Kuk and K. M. Ok, *Adv. Sci.*, 2025, **12**, 2414503.
8 Z. Chen, C. Liu, C. Li, J. Lu, Z. Yang, S. Pan and M. Mutailipu, *Adv. Opt. Mater.*, 2025, **13**, 2500631.
9 K. M. OK, *Acc. Chem. Res.*, 2016, **49**, 2774.
10 J. Lin, M. Lee, Z. Liu, C. Chen and C. Pickard, *Phys. Rev. B:Condens. Matter Mater. Phys.*, 1999, **60**, 13380.
11 C. Chen, Y. Wu, A. Jiang, B. Wu, G. You, R. Li and S. Lin, *J. Opt. Soc. Am. B*, 1989, **6**, 616.
12 C. T. Chen, G. L. Wang, X. Y. Wang and Z. Y. Xu, *Appl. Phys. B*, 2009, **97**, 9–25.
13 P. S. Halasyamani and J. M. Rondinelli, *Nat. Commun.*, 2018, **9**, 2972.
14 Y. F. Fu, W. D. Yao, Q. F. Huang, S. F. Yan, W. Liu and J. Wu, *Inorg. Chem.*, 2025, **64**, 15813–15817.
15 Y. F. Fu, W. D. Yao, J. J. Wu, Q. F. Huang, Y. M. Zhang, W. Zhou, W. Liu and S. P. Guo, *Small*, 2025, **21**, 2412173.
16 Y. Zhang, Q. Ding, Y. Li, Y. Li, X. Song, W. Huang, Y. Zhou, Q. Shao, Z. Bai, S. Zhao and J. Luo, *Laser Photonics Rev.*, 2025, **19**, 2500368.
17 Y. Liu, X. Liu, S. Liu, Q. Ding, Y. Li, L. Li, S. Zhao, Z. Lin, J. Luo and M. Hong, *Angew. Chem., Int. Ed.*, 2020, **59**, 7793–7796.
18 F. Kong, C. L. Hu, M. L. Liang and J. G. Mao, *Inorg. Chem.*, 2016, **55**, 948–955.
19 H. Wu, Z. Wei, Z. Hu, J. Wang, Y. Wu and H. Yu, *Angew. Chem., Int. Ed.*, 2024, **63**, e202406318.
20 Y. Song, M. Luo, C. Lin and N. Ye, *Chem. Mater.*, 2017, **29**, 896–903.
21 R. K. Li and Y. Ma, *CrystEngComm*, 2012, **14**, 5421–5424.
22 K. Yang, D. Wang, C. Zhu, K. Wu, G. Liu, J. Wang and C. Shen, *Mater. Today Chem.*, 2025, **48**, 102916.
23 X. Hao, C. S. Lin, M. Luo, Y. Q. Zhou, N. Ye and E. Shangguan, *Inorg. Chem.*, 2023, **62**, 7611–7616.
24 X. Hao, C. S. Lin, N. Ye, D. H. Lin, D. Zhao, Y. Q. Zhou, E. Shangguan and M. Luo, *Cryst. Growth Des.*, 2023, **23**, 362–368.
25 J. M. Zhao, H. K. Liu, X. D. Zhang, B. B. Zhang and Y. Wang, *CrystEngComm*, 2020, **22**, 6495–6501.
26 M. J. Li, X. Zhang, Z. Y. Xiong, Y. Q. Li, Y. Zhou, X. Chen, Y. P. Song, M. C. Hong, J. H. Luo and S. G. Zhao, *Angew. Chem., Int. Ed.*, 2022, **61**, e202211151.
27 M. Mutailipu, J. Han, Z. Li, F. Li, J. Li, F. Zhang, X. Long, Z. Yang and S. Pan, *Nat. Photonics*, 2023, **17**, 694–701.
28 Y. Wu, Y. Li, Y. Zhang, B. Teng, X. Jiang, C. Hu, S. Sun, L. Cao, J. Ma, K. Xu, D. Xu, Z. Lin and D. Zhong, *Adv. Funct. Mater.*, 2025, **35**, 2503125.
29 Y. Kang, C. Yang, J. Gou, Y. Zhu, Q. Zhu, W. Xu and Q. Wu, *Angew. Chem., Int. Ed.*, 2024, **63**, e202402086.
30 Q. Zhu, Y. Tao, C. Yang, J. Gou, Y. Zhu, X. Wang and Q. Wu, *Inorg. Chem.*, 2024, **63**, 22620–22627.
31 Y. Zhu, J. Gou, C. Yang, Q. Zhu, Y. Xiong and Q. Wu, *Angew. Chem., Int. Ed.*, 2025, **64**, e202509290.
32 X. Wen, Y. Yan, J. Lu, X. Shi, P. Tang, J. Chen, G. Yang, G. Peng, H. Yu, H. Zhang, Z. Hu, J. Wang and N. Ye, *Angew. Chem., Int. Ed.*, 2025, **64**, e202424153.
33 H. Yu, J. Young, H. Wu, W. Zhang, J. M. Rondinelli and P. S. Halasyamani, *Chem. Mater.*, 2017, **29**, 1845–1855.
34 P. Wang, Q. Huang, X. Meng, L. Liu, Q. Wu and H. Liu, *Inorg. Chem. Front.*, 2026, **13**, 2843–2853.
35 C. T. Chen, Y. C. Wu and R. K. Li, *Int. Rev. Phys. Chem.*, 1989, **8**, 65–91.
36 J. X. Zhang, Q. G. Yue, S. H. Zhou, X. T. Wu, H. Lin and Q. L. Zhu, *Angew. Chem., Int. Ed.*, 2024, **63**, e202413276.
37 P. Yu, L. M. Wu, L. J. Zhou and L. Chen, *J. Am. Chem. Soc.*, 2014, **136**, 480.
38 J. Cheng, G. Yi, Z. Zhang, Y. Long, H. Zeng, L. Huang, G. Zou and Z. Lin, *Angew. Chem., Int. Ed.*, 2024, **63**, e202318385.
39 Y. P. Xia, *N. Cryst. Struct.*, 2023, **238**, 799–800.
40 C. Shen, J. Liu, D. Sun, K. Yang, B. Zhang, K. Wu, J. Wang and D. Wang, *Small*, 2025, **21**, 2501471.
41 J. Chen, H. Y. Wu, M. B. Xu, M. C. Wang, Q. Q. Chen, B. X. Li, C. L. Hu and K. Z. Du, *Inorg. Chem. Front.*, 2024, **11**, 5587–5597.
42 D. X. Yang, Y. L. Lv, J. D. Guo, W. Y. Gao, W. Liu and R. L. Tang, *Inorg. Chem.*, 2025, **64**, 3643–3648.
43 S. K. Kurtz and T. T. Perry, *J. Appl. Phys.*, 1968, **39**, 3798–3813.

44 T. Chen, Z. Sun, X. Liu, J. Wang, Y. Zhou, C. Ji, S. Zhang, L. Li, Z. N. Chen and J. Luo, *J. Mater. Chem. C*, 2014, **2**, 8723–8728.
45 D. Yan, M. M. Ren, F. F. Mao, Y. Ma, R. L. Tang, B. Zhang, Y. Ma, X. D. Zhang and S. F. Li, *Inorg. Chem.*, 2023, **4**, 1323–1327.
46 L. Zhang, X. Zhang, F. Liang, Z. Hu and Y. Wu, *Inorg. Chem.*, 2023, **62**, 14518–14522.
47 X. Li, P. Gong, M. Chen, S. Zhuang, M. Qi, W. Wang, X. Wang, Z. Jia and M. Xia, *Inorg. Chem. Front.*, 2025, **12**, 7675–7683.
48 L. Li, H. Wu, H. Yu, Z. Hu, J. Wang and Y. Wu, *Mater. Today Chem.*, 2024, **42**, 102417.
49 J. Wu, Y. F. Fu, W. Liu and S. P. Guo, *Inorg. Chem. Front.*, 2024, **11**, 7090–7097.
50 J. Lu, Y. K. Lian, L. Xiong, Q. R. Wu, M. Zhao, K. X. Shi, L. Chen and L. M. Wu, *J. Am. Chem. Soc.*, 2019, **141**, 16151–16159.
51 R. W. Godby, M. Schluter and L. J. Sham, *Phys. Rev. B: Condens. Matter Mater. Phys.*, 1987, **36**, 6497–6500.
52 J. P. Perdew and Y. Wang, *Phys. Rev. B:Condens. Matter Mater. Phys.*, 1992, **45**, 13244–13249.
53 M. J. Dodge, *Appl. Opt.*, 1984, **23**, 1980–1985.
54 D. E. Zelmon, D. L. Small and D. Jundt, *J. Opt. Soc. Am. B*, 1997, **14**, 3319–3322.
55 (*a*) CCDC 2521794: Experimental Crystal Structure Determination, 2026, DOI: 10.5517/ccdc.csd.cc2qn46r; (*b*) CCDC 2522224: Experimental Crystal Structure Determination, 2026, DOI: 10.5517/ccdc.csd.cc2qnl22.